Influence of the carbon incorporation on the mechanical properties of TiB_2 thin films prepared by HiPIMS

N. Sala[1], M.D. Abad[*,1], J.C. Sánchez-López[2], F. Crugeira[1], A. Ramos-Masana[1], C. Colominas[1,3]

[1]*Grup d'Enginyeria de Materials (GEMAT), Institut Químic de Sarrià, Universitat Ramon Llull, Via Augusta 390, Barcelona 08017, Spain*
[2]*Instituto de Ciencia de Materiales de Sevilla, CSIC-Universidad de Sevilla, Avda. Américo Vespucio 49, 41092 Sevilla, Spain*
[3]*Flubetech S.L. Carrer Montsià 23, 08211 Castellar del Vallès, Barcelona, Spain*

**Corresponding authors:* manuel.abad@iqs.url.edu

Abstract

Nanostructured TiB_2 and TiBC thin films with carbon contents up to 11 at. % were prepared by physical vapor deposition using high power impulse magnetron sputtering (HiPIMS) technology. The influence of carbon incorporation during the deposition of TiB_2 coatings was investigated on the chemical composition, microstructure and mechanical properties by means of scanning electron microscopy, atomic force microscopy, x-ray photoelectron spectroscopy (XPS), x-ray diffraction (XRD), nanoindentation, scratch test, calotest and adhesion Daimler-Benz test. The results indicated that small additions of carbon up to 3 at. % improved the mechanical behavior and increased the adhesion of the TiB_2 thin films. Hardnesses up to 37 GPa were reached and the adhesion of the coating to AISI D2 steel substrates increased from 11 to 18 N. XRD and XPS results showed that the carbon atoms are either occupying interstitial sites within the hexagonal structure of the TiB_2 or forming bonds with titanium and boron atoms. The preferred orientation of the films determined by XRD also changed with the increasing carbon content in the (001) crystalline plane.

Keywords

HiPIMS; TiB_2; Thin Films; Hardness; Ti-B-C

1. Introduction

Surface engineering has introduced a great number of improvements in the use of materials for industrial applications. There is a growing interest in the development of advanced coatings as they allow the improvement of surface performances, whose lifetime is very limited under specific conditions. Ceramic coatings such as diamond-like carbon (DLC), borides and nitrides prepared by different deposition techniques present high hardness, good chemical resistance and high thermal stability [1–5]. One of the newest and promising techniques for depositing these coatings is high power impulse magnetron sputtering (HiPIMS) [6]. This technique is a magnetron sputtering based technique, in which a high power density is applied to the target in the form of very short pulses (~100 μs) providing a high degree of ionization of the specimens present in the plasma and, as a consequence, a change in the properties of the films such as denser and featureless structures [7].

TiB_2 has been widely studied for its good properties such as high hardness between 25-35 GPa, good chemical stability and high melting point (>3000ºC) [2,6,8–11]. which make it an excellent candidate as protective coating. The main problem of these coatings is the high internal tensions that can cause fracture of the film and also high friction coefficient [10]. The introduction of carbon in these structures is a good approach to reduce friction and wear, extending the lifetime of these coatings [12–15]. These Ti-B-C systems, also called TiB_xC_y, have been deposited and studied by several techniques such as high pressure spark plasma sintering [16], thermo reactive diffusion [17], ion beam deposition [18], pulsed laser ablation [19], chemical vapor deposition [20] and magnetron sputtering [12,14,15,21–23]. HiPIMS technology has been applied to produce TiB_2 thin films, but the study of the incorporation of the carbon over TiB_2 prepared by HiPIMS has not been described yet [6,24].

In the present work, the influence of the addition of carbon on TiB_2 films sputtered via HiPIMS is studied. The thin films were prepared by multi-target magnetron sputtering using two graphite targets and two TiB_2 targets. The TiB_2 targets were used in HiPIMS and the graphite targets in direct current (DC) mode. The power densities applied to the graphite and TiB_2 targets were fixed, while the carbon content was controlled by the graphite sputtering time. Very high harnesses are reached due to the formation of nanocrystalline hard TiB_2 phase and the inclusion of C in the TiB_2 forming additional hard TiB_xC_y phases. Accordingly, the microstructural evolution and the variation of the mechanical properties of the TiBC thin films were systematically investigated.

2. Materials and methods

The TiB_2-TiBC coatings in this study were prepared using a CemeCon CC800/9 ML equipment. The TiB_2-TiBC coatings were grown onto silicon wafer and mirror polished AISI D2 steel by argon sputtering of TiB_2 and graphite targets (CemeCon 99.965% purity). The magnetrons were connected to HiPIMS (TiB_2) and DC power sources (graphite), at sputtering powers of 4.5 kW and 1 kW, respectively. The HiPIMS pulse parameters were the following: a duty cycle of 5.5 %, a duration of 70 μs and a repetition frequency of 800 Hz. The potential of the substrate holder was operated at 70 V. The background pressure was 3×10^{-3} Pa and the working pressure was set in a range of 0.3 to 0.45 Pa. The sputtering times are summarized in Table 1. Sample C1 was prepared by sputtering the TiB_2 target. In sample C2, after sputtering the TiB_2 target for 3 hours, the introduction of carbon was carried out during the last 30 minutes of the deposition by switching on the graphite target leading to a co-deposition of C and TiB_2. In sample C3, the TiB_2 and graphite targets were co-sputtered during the whole process.

The elemental composition of the samples was analysed by electron probe microanalysis (EPMA) using a JEOL JXA-8200 SuperProbe equipment. Scanning electron microscopy (SEM) observations were done with a SEM FEG Hitachi S4800 equipment. The roughness and microstructure of the deposited coatings on silicon substrate was determined with an AFM Nano-Observer CSInstruments in contact mode. X-ray photoelectron spectroscopy (XPS) spectra were measured using a SPECS Phoibos 150 MCD instrument using non-monochromatic Cu K_α radiation (1253.6 eV) as X-ray excitation source. The measurements were performed in constant analyser energy mode with a 35 eV pass energy for high resolution spectra of the detected elements. Samples were previously subjected to Ar^+ ion bombardment at $\approx 6\times10^{-5}$ mbar (2.70 KeV y 10 mA) for 15 min to partially remove the contaminant layer. A fitting analysis was performed by a least squares fit of the C 1s of the films of the different carbon bonds (carbides, C–C, C-OH) in accordance to previous works [14,15]. The crystal structure of the films was examined by x-ray diffraction analysis (XRD) in Bragg-Brentano and grazing incidence (GIXRD) geometries using Cu K_α radiation by a diffractometer Empyrean coupled with a PIXcel Medipix 3 detector manufactured by Philips Panalytical (now Malvern Panalytical GmbH, United Kingdom). GIXRD scans were collected with a constant angle of incidence of 0.5° and 1°, respectively, in order to avoid intense signals from the substrate and obtain stronger signals from the coatings. The crystalline phases were determined with X'Pert Highscore software. In order to investigate the texture development as a function of the carbon content, the texture coefficient was calculated from their respective XRD peaks with the following formula [24].

$$T(hkl) = \frac{I(hkl)}{I(001) + I(100) + I(101)} \quad (1)$$

Where T refers to the orientation parameter; (hkl) refers to the corresponding diffracting lattice planes.

Thickness and adhesion quality of the films were studied with a CemeCon Kalottchen/L equipment using a cemented carbide ball of 30 mm diameter and a diamond suspension of 0.25 μm particle size for 45 seconds. The adhesion of the films was also investigated by the Daimler-Benz test and more quantitatively by scratch testing at increasing load. In the first technique a Rockwell-C indenter was applied with a force of 150 Kp and the indentations were observed using an optical microscope Leica DM50M coupled with an ICC50 HD camera. The scratch tests were carried out using a TRIBOtechnic Millenium 200 scratch-tester. A Rockwell C diamond tip (200 μm radius) was drawn over the coated surface for 8 mm-length as the applied normal load increased continuously up to 30 N. The diamond tip was cleaned after each scratch and the test was repeated twice on each sample. Acoustic emissions were recorded during the scratching, but optical microscopy was applied to assess the critical normal load values and to indicate the coating fracture and delamination modes. The hardness (H) and reduced Young modulus (E_r) of the films were measured using a nanoindententer tester (Nanoindenter XP MTS) with a Berkovich diamond indenter.

3. Results and discussion

3.1. Elemental composition and structural characterization

The elemental compositions of the coatings obtained by EPMA are summarized in Table 1. The carbon content varied from 0 to 11 at. %. The carbon content in the sample C2 is relatively low (~ 3 at. %), as carbon was added only in the last step of the coating deposition. In C3 sample, carbon was added from the beginning of the synthesis and a value of 11 at. % is reached. The oxygen content ranged from 2 to 8 at. % in the coatings, in agreement with the reported bibliography of other authors preparing TiB_2 by HiPIMS [6,24].

Fig. 1 shows SEM micrographs of the cross-sections (left) and AFM surface images (right) of the samples deposited. The three samples were characterized by a dense structure and fine columns, with no significant differences among them. Despite

the carbon addition during the last step of the deposition process, no bilayer structure (or multilayer) could be identified in sample C2. Similar morphologies on TiB_2 coatings prepared by HiPIMS were reported by Zhang *et al.* [24]. The AFM top surface images (scanning area = 10 µm x 10 µm) shown in Fig. 1 reveal very smooth surfaces. The RMS roughness of the prepared coatings is shown in Table 1. The highest value (5.6 nm) corresponds to the pure TiB_2 film while the incorporation of carbon leads to a progressive decrease on the roughness (from 5.6 to 2.3 and 1.5 nm). These roughness values are similar to those found by Zhang *et al.* [24] for TiB_2 coatings and lower than those reported by Contreras *et.al.* for TiBC films deposited by DC-MS [23].

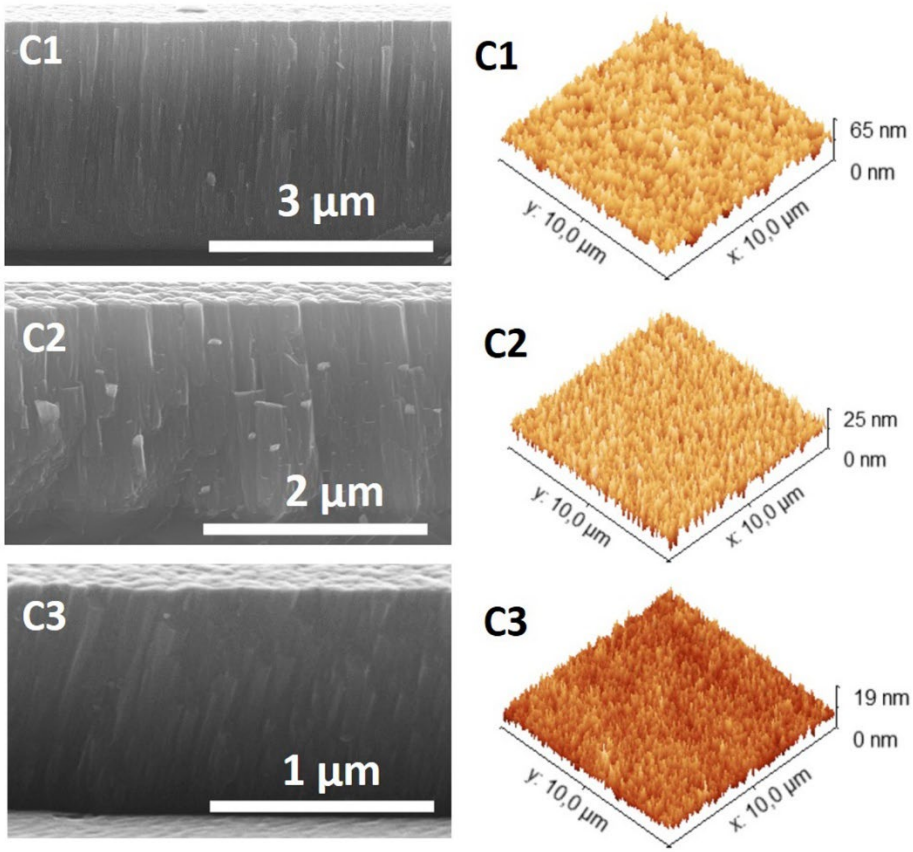

Figure 1. SEM cross-section images (left) and AFM top-view images (right) of the studied thin films.

The XPS spectroscopy analysis allow us to investigate the chemical bonding structure. Fig. 2a shows the B 1s photoelectron spectra for the three coatings. The chemical bonding located at 188.0 eV is assigned to the B-Ti bonds in C1 sample (as there is no carbon on the sample). Interestingly, the spectrum of sample C3 shows a shift of 0.2 eV to higher binding energies which is in agreement with the incorporation of a more electronegative element, such as carbon, and therefore it is assigned to the B-C bonds. [22]. This displacement of the B 1s peak position was also observed by Baker in TiBC thin films with growing C contents [25].

Fig. 2b displays the three main component peaks considered in the fitting analysis of C 1s XPS peak for sample C3 (as representative of coating C2 and C3) at 283.0, 284.6 and 286.0 eV. The peak at 283.0 eV can be assigned to a carbon atom bonded to both Ti and B forming a titanium boride-carbide phase (TiB_xC_y) as previously reported by other authors [12,14]. The components at 284.6 and 286.0 eV can be ascribed to carbon bonded to carbon (C-C) and hydroxide groups (C-OH), respectively, from the hydrocarbon contamination layer formed by the air exposure. The absence of a segregated amorphous C-C phase was proved by micro-Raman analysis (results not shown), in agreement with the low carbon concentration inside the samples. Based on these results, carbon atoms in Ti-B-C coatings, are whether occupying interstitial sites within the hexagonal structure of the TiB_2 or forming bonds with titanium and boron atoms, but not in a free state in form of amorphous carbon.

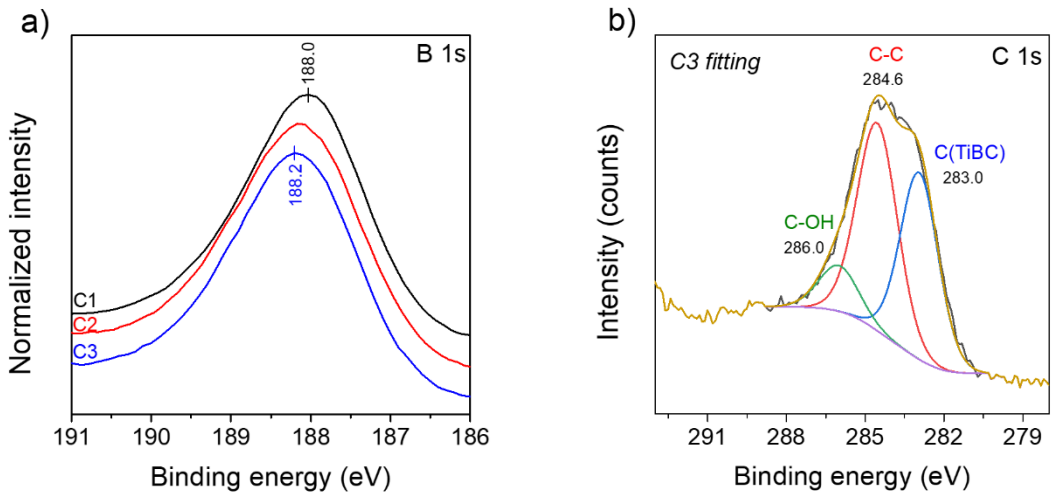

Figure 2 (a) XPS spectra of the B1s photoelectron peak for the coatings and (b) a representative example of the XPS fitting of the C 1s for the coating C3.

Fig. 3 depicts the diffractograms in the Bragg-Bentano and grazing incidence geometry at 0.5º, 1º and 2θ degrees. The analysis of the diffractograms allowed the identification of the following phases: TiB_2 (JCPDS card nº 075-0967), and the substrate AISI D2 steel (JCPDS card 006-4192). The three coatings show well-defined peaks, centered at 27.8, 34.1 and 44.6 º that correspond respectively to the crystallographic planes (001), (100) and (101) of the TiB_2 hexagonal phase. The peak corresponding to the plane (101) overlaps with the plane (011) of Fe originating from the D2 substrate [23], this effect can be minimized with the 1 and 0.5º GIXRD measurements, as the signals corresponding to the substrate are removed. The (001) diffraction peaks from the samples with carbon, specially C3, shift towards lower 2θ angles in comparison to the standard pattern and C1. This can be due to the intrinsic residual stress of the thin film and/or the C incorporation in the interstitial spaces in the atomic cell [14]. If the carbon is introduced occupying the interstices of the cell, the cell size increases so the displacement of the peaks is observed at smaller angles [23]. No carbon-rich phases in the form of metal carbides are detected in the diffractograms, which again suggest that the carbon incorporated in the coating is found in the form of solid solution or occupying interstices within the crystalline lattice of TiB_2. These results are consistent with those obtained for the XPS spectra.

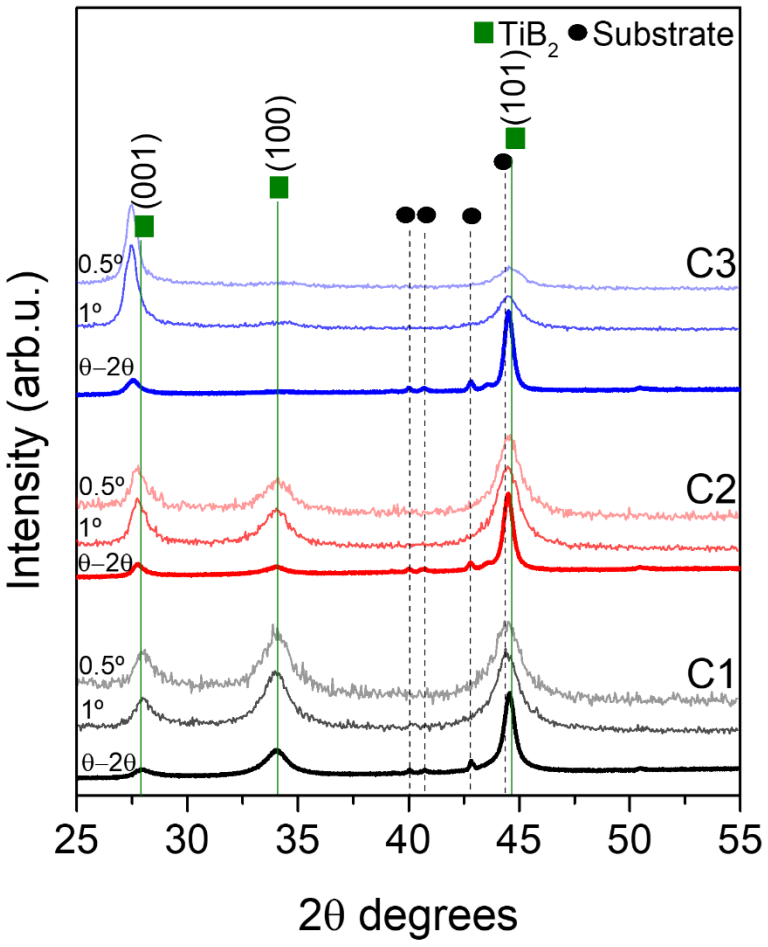

Figure 3. XRD and GIXRD diffractograms at Bragg-Bentano and 0.5 and 1 º configurations for the studied coatings.

GIXRD diffractograms show a clear change in the relative intensities of the different peaks as a function of the deposition process. The texture coefficient has been calculated as explained in materials and methods section and the values are shown in Table 1 and represented in Fig 4a. In the sample prepared without carbon, a combination of different texture components (preferred crystallite orientation) of the lattice planes (001), (100) and (101) parallel to the substrate surface is observed. In C2, where the carbon was added just for 30 minutes, the most significant change is the decrease of the (100). In C3, where

the carbon was added from the beginning of the deposition process, the (100) orientation almost disappears and the (001), which is the most densely packed plane and thus possesses the lowest surface energy, becomes preferential [24,26].

In addition, the crystallite size was estimated using the Scherrer equation for the different crystallographic planes as shown in Table 1 and Fig. 4b. The comparison of the values obtained from the (100) and (101) planes show minor variations in the crystallite size for the different coatings (varying from 3 to 5 nm and 6 to 7 nm respectively). In contrast, the (001)-oriented crystallites grow from 8 to 14 nm as the carbon content increased from 3 to 11 at. %. Similar crystallite sizes have been reported for TiBC thin films with carbon contents around 5-8 at. % [22]. The results obtained for the texture development and crystallite size are consistent with the changes observed during the modification of the bias voltage reported by Zhang *et al.* [24]. In addition, the low carbon concentrations attained in these coatings reduce the trend towards amorphization of the TiB_2 phase as observed in TiBC coatings with higher carbon contents [14].

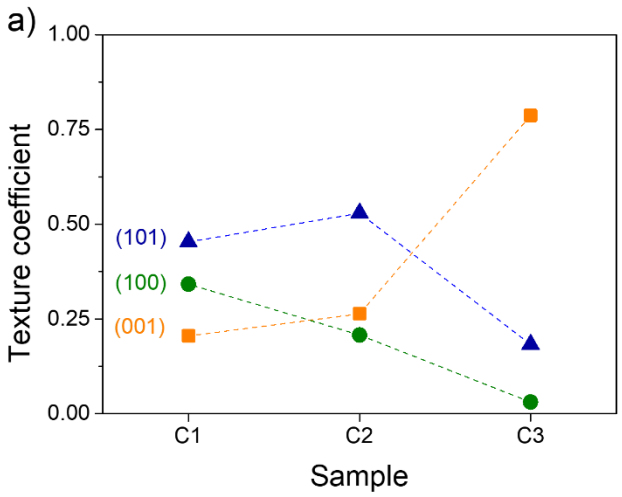

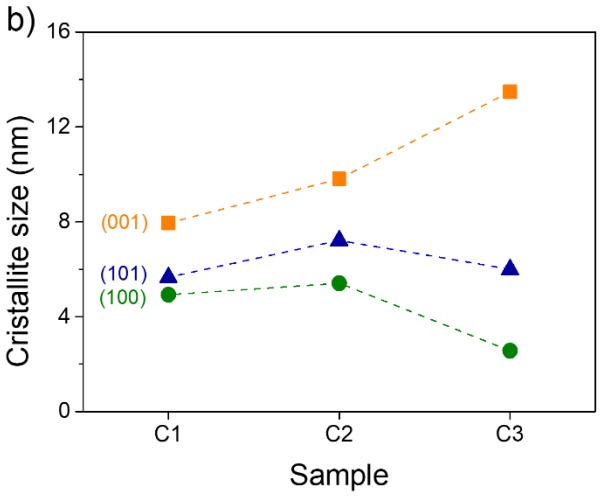

Figure 4. Texture coefficient development (a) and crystallite size (b) of the prepared coatings.

3.2. Mechanical characterization

The Daimler–Benz Rockwell-C (HRC-DB) adhesion test is a commercially adopted method to evaluate film/substrate adhesion quality which has grown relevance during the last years [27–29]. By observing the indentation marks, adhesion properties can be classified into two groups: H1-H4 acceptable, H5-H6 not suitable [29]. The inspection of the indentations in the coatings (Fig. 5a) allows to determine H1, H2 and H3 adhesion quality for the samples C1, C2 and C3 respectively. The adhesion is acceptable for all the samples and no delamination are observed. Samples C1 and C2 show radial cracks around the crater, indicative of high hardness and brittleness for both coatings. In C3 sample, the adhesion is not so good as inferred from the presence of branched cracks but still acceptable.

Ball cratering measurements were performed with the aim of determining the resultant thickness of the coatings, and studying the abrasion resistance [30], as can be appreciated in Fig. 5b. The values of the thickness match with the ones obtained by cross-section SEM (Table 1). Visual assessment of the craters in Fig. 5b does not show any perceptible difference in the wear behaviour in the whole section of the coating which confirms that the thin films are homogeneous, even the sample C2 which had a two-step deposition process.

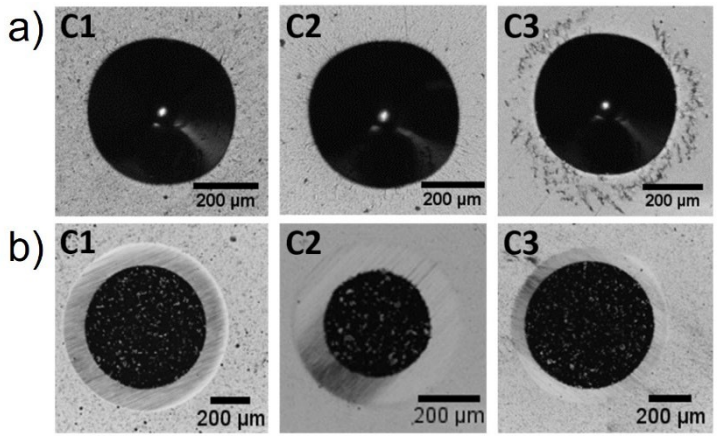

Figure 5. a) Photomicrographs of the pits in the coatings surface after a Daimler-Benz test on the samples. b) Images of craters grided by ball crater micro-abrasion method (Calotest) of the different coatings.

The type of failure which is observed by scratch-tests for a given coating-substrate system depends on the test load, the coating thickness, the residual stress and the properties of the substrate (e.g. hardness), as well as on test parameters such as indenter radius and sliding speed [31]. The scratch test marks have been etched with Heyn's reagent to reveal the presence of the substrate and thus detect the failure of the coating (Fig. 6). Different types of coating damages can be observed according to [31] [32]. L_{c1} and L_{c2} are respectively defined as the load at which the first cracking occurs, and the load at which catastrophic failure begins. In C1 sample, gross spallation (brittle fracture) is observed and *the* catastrophic failure (L_{c2}) is determined to be at 11.0±0.5 N. This can denotate poor adhesion and/or high residual stress of the coatings. C2 and C3 samples however present a different failure mechanism associated to buckling and spallation. The composition of these coatings (TiB_2 and TiB_xC_y phases) allow the stress generated by the moving indenter to be released by buckling the coating. In C2 where the TiB_xC_y phase was formed only in the last step on deposition process, the buckling spreads laterally by the propagation of an interfacial crack results in spallation. The higher carbon content, and therefore, TiB_xC_y formation across the entire thickness in C3, led to restricted crack propagation and no clear signs of buckle spallation are observed.

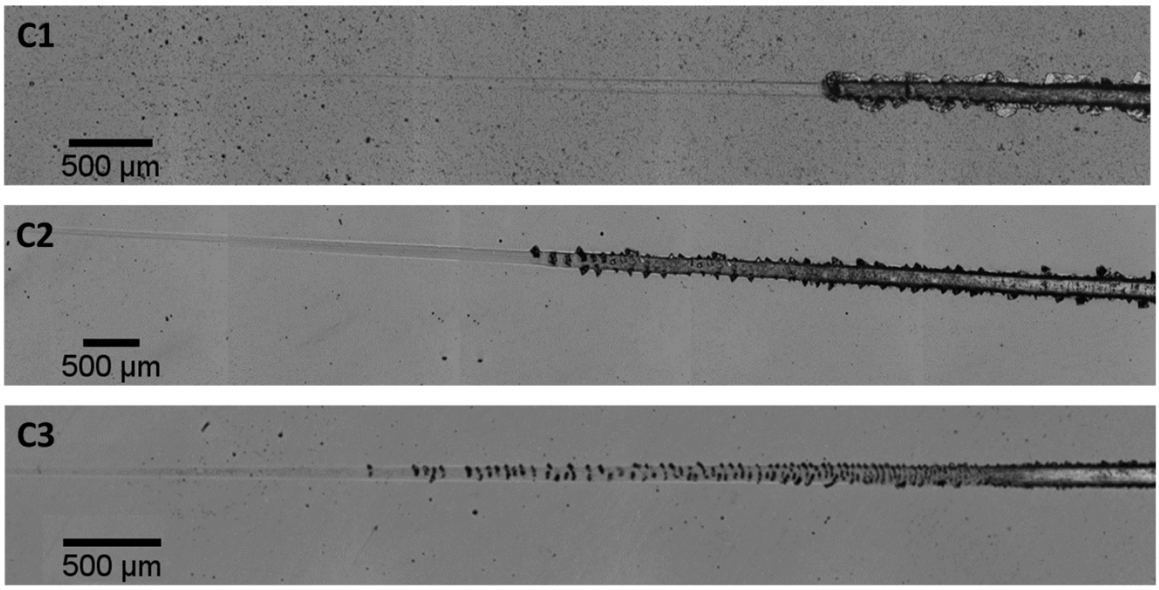

Figure 6. SEM images show scratch tracks and the failure of the coatings.

The critical loads for C2 are L_{c1} 12.8 ± 1.2 N and L_{c2} 16.1 ± 0.3 N, and for C3 are L_{c1} 6.31 ± 0.1 N and L_{c2} 18.2 ± 0.8 N. Fig. 7 displays the L_{c1} and L_{c2} results for the coatings. Similar L_c values varying from 8 to 17 N were found by Contreras *et al.* for TiBC thin films [23]. The TiB_2 coating (C1) exhibit the lowest critical load, attributed to the hard and brittle character of TiB_2. The incorporation of carbon has led a significant increase of the interfacial adhesion, up to 50 % with respect to the TiB_2 coating. The carbon incorporation in the films modifies the failure mechanism, as the crack formation appears at lower loads, but the final breakage occurs at higher loads. These values are still low in comparison to other coatings reported in the literature [33], which could be enhanced by previous deposition of an anchoring layer such as Ti or TiN.

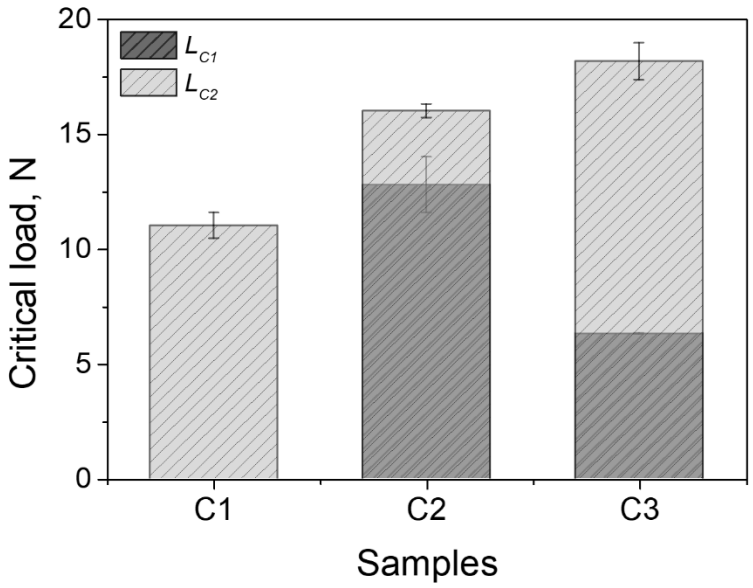

Figure 7. L_{C1} and L_{C2} for the prepared coatings

Hardness and reduced Young modulus of the coatings were measured by nanoindentation. Hardness values vary between 26 and 37 GPa and reduced Young modulus between 365 and 447 GPa depending on the sample and the carbon concentration (Table 1). Both C2 and C3 present higher hardness than C1, which shows that the addition of carbon in the structure improve the mechanical properties (Fig. 8). Contreras *et al.* [23] reported a similar trend with low carbon incorporations and concomitant shift of the (001) TiB_2 diffraction peak. Higher carbon concentrations lead to a decrease of the hardness values because of the favoured formation of an amorphous C (a-C) phase although it results in an enhancement of the tribological properties. Abad *et al*. showed a correlation of the hardness with the formation of a ternary TiB_xC_y phase and the reduction of coefficient of friction by increasing the a-C fraction [15]. In the present research, we show that a small addition of carbon is assimilated into the crystal structure of TiB_2 leading to the formation of the phase TiB_xC_y which correlates with the hardness increment. The reduced Young modulus decreases slightly, but it is still quite high. The consequence increase in the H/E ratio (Table 1) helps to increase fracture toughness [34,35], as demonstrated by enhanced resistance to crack propagation in parallel to TiB_xC_y formation.

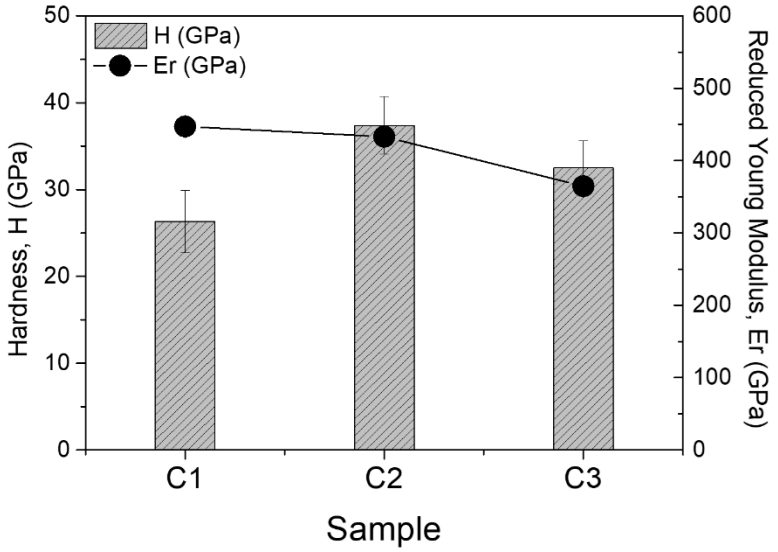

Figure 8. Hardness (H) and reduced Young modulus (E_r) of the prepared samples.

4. Conclusions

TiBC coatings have been successfully deposited using the HiPIMS technique with the introduction of up to 11 at. % carbon in the structure. Thanks to the additional ion bombardment provided by this technique the coatings appear to be very smooth and compact. The microstructure is formed by very fine columns and the average roughness parameters are in the range of 1-6 nm. The B 1s and C 1s XPS peaks confirm the formation of a mixed TiB_xC_y phase where carbon is bonded to boron and titanium. The displacement of the XRD peaks to smaller angles with the carbon incorporation matches with the expansion of the unit cell due to carbon incorporation in the TiB_2 lattice. In addition, a preferential orientation to the most densely packed plane (001) and increased crystallization is denoted in parallel to the TiB_xC_y formation. The addition of carbon in the structure modifies the fracture mechanism, and improves the adhesion to the substrate. While in pure TiB_2 a catastrophic failure is observed around 11 N load value, in TiB_2/TiBC and TiBC films, restricted crack propagation and no clear signs of buckle spallation are observed. The benefits of small addition of carbon (up to 11 at. %) is also manifested in a hardness increment with values ranging between 32 and 37 GPa.

Acknowledgments

This research was supported by "La Caixa Fundation" [2017-LC-07], "Secretaria d'Universitats i Recerca (SUR) del Departament d'Empresa I Coneixement (DEC) de la Generalitat de Catalunya" and "Fons Socials Europeus [2019FI_B01190] [2020FI_B1_00114] [2021FI_B2_00167] [2020-URL-Proj-020] [2021-URL-Proj-019]".

References

[1] J. Robertson, Diamond-like carbon, Pure Appl. Chem. 66 (1994) 1789–1796. https://doi.org/10.1351/pac199466091789.

[2] M. Mikula, B. Grančič, V. Buršíková, A. Csuba, M. Držík, Š. Kavecký, A. Plecenik, P. Kúš, Mechanical properties of superhard TiB2 coatings prepared by DC magnetron sputtering, Vacuum. 82 (2007) 278–281. https://doi.org/10.1016/j.vacuum.2007.07.036.

[3] O. Knotek, F. Jungblut, R. Breidenbach, Magnetron-sputtered superhard coatings within the system TiBCN, Vacuum. 41 (1990) 2184–2186. https://doi.org/10.1016/0042-207X(90)94220-K.

[4] P. Souček, J. Daniel, J. Hnilica, Superhard nanocomposite nc-TiC/a-C:H coatings: The effect of HiPIMS on coating microstructure and mechanical properties, Surf. Coatings Technol. 311 (2017) 257–267. https://doi.org/10.1016/j.surfcoat.2017.01.021.

[5] Q. Ma, L. Li, Y. Xu, X. Ma, Y. Xu, H. Liu, Effect of Ti content on the microstructure and mechanical properties of TiAlSiN nanocomposite coatings, Int. J. Refract. Met. Hard Mater. 59 (2016) 114–120. https://doi.org/10.1016/j.ijrmhm.2016.06.005.

[6] N. Nedfors, A. Mockute, J. Palisaitis, P.O.Å. Persson, L.Å. Näslund, J. Rosen, Influence of pulse frequency and bias on microstructure and mechanical properties of TiB2 coatings deposited by high power impulse magnetron sputtering, Surf. Coatings Technol. 304 (2016) 203–210. https://doi.org/10.1016/j.surfcoat.2016.06.086.

[7] J.T. Gudmundsson, N. Brenning, D. Lundin, U. Helmersson, High power impulse magnetron sputtering discharge, J. Vac. Sci. &Technology. A. Vacuum, Surfaces, Film. (2012).

[8] B. Basu, G.B. Raju, A.K. Suri, Processing and properties of monolithic TiB2 based materials, Int. Mater. Rev. 51 (2006) 352–374. https://doi.org/10.1179/174328006X102529.

[9] B. Grančič, M. Mikula, L. Hrubá, M. Gregor, M. Štefečka, A. Csuba, E. Dobročka, A. Plecenik, P. Kúš, The influence of deposition parameters on TiB2 thin films prepared by DC magnetron sputtering, Vacuum. 80 (2005) 174–177. https://doi.org/10.1016/j.vacuum.2005.08.013.

[10] N. Panich, Y. Sun, Mechanical properties of TiB2-based nanostructured coatings, Surf. Coatings Technol. 198 (2005) 14–19. https://doi.org/10.1016/j.surfcoat.2004.10.096.

[11] M. Saeedi Heydari, H.R. Baharvandi, Comparing the effects of different sintering methods for ceramics on the physical and mechanical properties of B4C-TiB2 nanocomposites, Int. J. Refract. Met. Hard Mater. 51 (2015) 224–232. https://doi.org/10.1016/j.ijrmhm.2015.04.003.

[12] M.D. Abad, D. Cáceres, Y.S. Pogozhev, D.V. Shtansky, J.C. Sánchez-López, Bonding structure and mechanical properties of Ti-B-C coatings, Plasma Process. Polym. 6 (2009) 107–112. https://doi.org/10.1002/ppap.200930403.

[13] J.C. Sánchez-López, D. Martínez-Martínez, M.D. Abad, A. Fernández, Metal carbide/amorphous C-based nanocomposite coatings for tribological applications, Surf. Coatings Technol. 204 (2009) 947–954. https://doi.org/10.1016/j.surfcoat.2009.05.038.

[14] J.C. Sánchez-López, M.D. Abad, A. Justo, R. Gago, J.L. Endrino, A. García-Luis, M. Brizuela, Phase composition and tribomechanical properties of Ti-B-C nanocomposite coatings prepared by magnetron sputtering, J. Phys. D. Appl. Phys. 45 (2012). https://doi.org/10.1088/0022-3727/45/37/375401.

[15] M.D. Abad, J.C. Sánchez-López, M. Brizuela, A. García-Luis, D.V. Shtansky, Influence of carbon chemical bonding on the tribological behavior of sputtered nanocomposite TiBC/a-C coatings, Thin Solid Films. 518 (2010). https://doi.org/10.1016/j.tsf.2010.04.038.

[16] L. Jaworska, M. Karolus, S. Cygan, J. Morgiel, J. Cyboroń, J. Laszkiewicz Łukasik, P. Putyra, Influence of pulsed current during high pressure sintering on crystallite size and phase composition of diamond with Ti–B bonding phase, Int. J. Refract. Met. Hard Mater. 70 (2018) 101–106. https://doi.org/10.1016/j.ijrmhm.2017.09.011.

[17] B. Kurt, L. Özdoğan, B. Güney, Ö.S. Bölükbaşı, A. Günen, Characterization and wear behavior of TiBC coatings formed by thermo-reactive diffusion technique on AISI D6 steel, Surf. Coatings Technol. 385 (2020) 125332. https://doi.org/10.1016/j.surfcoat.2020.125332.

[18] W. Dai, X. Gao, X. Li, Q. Wang, Influence of carbon incorporation on microstructure and properties of titanium diboride coatings deposited by combining ion beam with magnetron sputtering, Ceram. Int. 45 (2019) 22498–22505. https://doi.org/10.1016/j.ceramint.2019.07.273.

[19] H.Y. Zhai, H.M. Christen, C. Cantoni, A. Goyal, D.H. Lowndes, H.Y. Zhai, H.M. Christen, C. Cantoni, Epitaxial titanium diboride films grown by pulsed-laser deposition, 1963 (2002) 1–4. https://doi.org/10.1063/1.1461869.

[20] J.T. Ok, I.W. Park, J.J. Moore, M.C. Kang, K.H. Kim, Syntheses and mechanical properties of Ti-B-C coatings by a plasma-enhanced chemical vapor deposition, Surf. Coatings Technol. 200 (2005) 1418–1423. https://doi.org/10.1016/j.surfcoat.2005.08.078.

[21] J. Lauridsen, N. Nedfors, U. Jansson, J. Jensen, P. Eklund, L. Hultman, Ti-B-C nanocomposite coatings deposited by magnetron sputtering, Appl. Surf. Sci. 258 (2012) 9907–9912. https://doi.org/10.1016/j.apsusc.2012.06.049.

[22] J.C. Qian, Z.F. Zhou, W.J. Zhang, K.Y. Li, I. Bello, L. Martinu, J.E. Klemberg-Sapieha, Microstructure and tribo-mechanical properties of Ti-B-C nanocomposite films prepared by magnetron sputtering, Surf. Coatings Technol. 270 (2015) 290–298. https://doi.org/10.1016/j.surfcoat.2015.02.043.

[23] E. Contreras, Y. Galindez, M.A. Gómez, Microstructure, mechanical and tribological properties of TiBC coatings by DC magnetron sputtering onto AISI M2 steel using independent TiB2 and graphite targets, Surf. Coatings Technol. 350 (2018) 298–306. https://doi.org/10.1016/j.surfcoat.2018.05.079.

[24] T.F. Zhang, B. Gan, S. mo Park, Q.M. Wang, K.H. Kim, Influence of negative bias voltage and deposition temperature on microstructure and properties of superhard TiB2 coatings deposited by high power impulse magnetron sputtering, Surf. Coatings Technol. 253 (2014) 115–122. https://doi.org/10.1016/j.surfcoat.2014.05.023.

[25] M.A. Baker, Advanced characterisation of nanocomposite coatings, Surf. Coatings Technol. 201 (2007) 6105–6111. https://doi.org/10.1016/j.surfcoat.2006.08.118.

[26] J. Pelleg, G. Sade, M. Sinder, D. Mogilyanski, Compositional and structural changes in TiB2 films induced by bias, in situ and post-deposition annealing, respectively, Phys. B Condens. Matter. 381 (2006) 118–127. https://doi.org/10.1016/j.physb.2005.12.260.

[27] J.A. García, P.J. Rivero, E. Barba, I. Fernández, J.A. Santiago, J.F. Palacio, G.G. Fuente, R.J. Rodríguez, A comparative study in the tribological behavior of DLC coatings deposited by HiPIMS technology with positive pulses, Metals (Basel). 10 (2020). https://doi.org/10.3390/met10020174.

[28] S. Schmidt, T. Hänninen, J. Wissting, L. Hultman, N. Goebbels, A. Santana, M. Tobler, H. Högberg, SiNx coatings deposited by reactive high power impulse magnetron sputtering: Process parameters influencing the residual coating stress, J. Appl. Phys. 121 (2017). https://doi.org/10.1063/1.4977812.

[29] S. Mato, J.C. Sánchez-López, J. Barriga, F.J. Pérez, G. Alcalá, Insights into the role of the layer architecture of Cr–Ti–N based coatings in long-term high temperature oxidation experiments in steam atmosphere, Ceram. Int. 47 (2020) 4257–4266. https://doi.org/10.1016/j.ceramint.2020.10.003.

[30] F.J.G. Silva, R.C.B. Casais, R.P. Martinho, A.P.M. Baptista, Mechanical and tribological characterization of TiB2 thin films, J. Nanosci. Nanotechnol. 12 (2012) 9187–9194. https://doi.org/10.1166/jnn.2012.6759.

[31] S.J.Bull, Failure modes in scratch adhesion testing, Surf. Coatings Technol. 50 (1991) 25–32.

[32] S.J. Bull, Failure mode maps in the thin film scratch adhesion test, Tribol. Int. 30 (1997) 491–498. https://doi.org/10.1016/S0301-679X(97)00012-1.

[33] S. El Mrabet, M.D. Abad, J.C. Sánchez-López, Identification of the wear mechanism on WC/C nanostructured coatings, Surf. Coatings Technol. 206 (2011) 1913–1920. https://doi.org/10.1016/j.surfcoat.2011.07.059.

[34] J. Musil, J. Vlček, Magnetron sputtering of hard nanocomposite coatings and their properties, Surf. Coatings Technol. 142–144 (2001) 557–566. https://doi.org/10.1016/S0257-8972(01)01139-2.

[35] J. Musil, Hard nanocomposite coatings: Thermal stability, oxidation resistance and toughness, Surf. Coatings Technol. 207 (2012) 50–65. https://doi.org/10.1016/j.surfcoat.2012.05.073.

Table

Table 1: Summary of the deposition parameters and properties of the thin films.

Films	Sputtering time (h)		Elemental composition (at. %)			Thickness (µm)	Roughness (nm)	Texture coefficient	Grain size (nm)			Critical load (N)		H(GPa)	E_r (GPa)	H/E_r
	TiB_2	C	Ti	B	C			(001):(100):(101)	(001)	(100)	(101)	L_{c1}	L_{c2}			
C1-TiB_2	3.5	-	31	69	-	3.03	5.6	0.21:0.34:0.45	8	5	6	-	11±0.5	26.3±3.6	447±9	0.059
C2-TiB_2/TiBC	3.0	0.5	30	67	3	2.27	2.3	0.26:0.21:0.53	10	5	7	13±1.2	16±1.3	37.4±3.3	433±10	0.086
C3-TiBC	2	2	27	62	11	1.07	1.5	0.79:0.03:0.18	14	3	6	6.3±0.1	18±0.8	32.5±3.1	365±8	0.089